Capacitive-Piezoelectric Transducers for High-Q Micromechanical AlN Resonators

Li-Wen Hung, *Student Member, IEEE*, and Clark T.-C. Nguyen, *Fellow, IEEE*

***Abstract*— A capacitive-piezoelectric (also known as, capacitive-piezo) transducer that combines the strengths of capacitive and piezoelectric mechanisms to achieve a combination of electromechanical coupling and Q higher than otherwise attainable by either mechanism separately, has allowed demonstration of a 1.2-GHz contour-mode aluminum nitride (AlN) ring resonator with $Q > 3000$ on par with the highest measured d_{31}-transduced AlN-only piezoelectric resonators past 1 GHz, and a 50-MHz disk array with an even higher $Q > 12\,000$. Here, the key innovation is to separate the piezoelectric resonator from its metal electrodes by tiny gaps to eliminate metal material and metal-to-piezoelectric interface losses thought to limit thin-film piezoelectric resonator Q, while also maintaining high electric field strength to preserve a strong piezoelectric effect. While Q increases, electromechanical coupling decreases, but the $k_{\mathbf{eff}}^2 \cdot Q$ product can still increase overall. More importantly, use of the capacitive-piezo transducer allows a designer to trade electromechanical coupling for Q, providing a very useful method to tailor Q and coupling for narrowband radio frequency (RF) channel-selecting filters for which Q trumps coupling. This capacitive-piezo transducer concept does not require dc-bias voltages and allows for much thicker electrodes that reduce series resistance without mass loading the resonant structure. The latter is especially important as resonators and their supports continue to scale toward even higher frequencies. [2013-0395]**

***Index Terms*— Micromechanical resonator, quality factor, small gap, filter, oscillator, electromechanical coupling, equivalent circuit, self-alignment, aluminum nitride.**

I. Introduction

THE EVER-INCREASING appetite for wireless interconnectivity continues to drive research on paradigm-shifting communication modalities, such as software-defined and/or cognitive radio [1], both expected to enable more flexible, higher volume communications. Practical realization of such radios with reasonable power consumption, however, could benefit greatly from more advanced hardware capable of realizing radio frequency (RF) channel-selecting front-ends [2] and/or frequency gating spectrum analyzers [3]. Such advanced hardware in turn drive a need for high frequency resonators with simultaneous high Q (e.g., $>10\,000$ at 1 GHz) and low impedance (e.g., $<200\Omega$) as building blocks for narrow-band filters with percent bandwidths on the order of 0.1% or less. In brief, high Q is needed for low filter insertion loss; and low impedance (or more precisely, sufficient electromechanical coupling) for proper termination of the filter with minimal passband distortion [4]. Here, the electromechanical coupling of a given resonator is commonly gauged by some function of the ratio of its motional-to-static transducer capacitance (C_x/C_o). For example, the popular gauge for electromechanical coupling k_{eff}^2 is essentially equal to (C_x/C_o) for low values [5]. In practical terms, a 0.1%-bandwidth, 0.5dB-ripple, 3-resonator Chebyshev filter requires a minimum (C_x/C_o) $\sim$ 0.25% to maintain passband distortion less than 0.5dB over the designed 0.5dB ripple. A two-resonator version requires only 0.15%.

Fortunately, the (C_x/C_o) requirement shrinks with bandwidth. So an RF channel-selecting filter with a percent bandwidth of only 0.1% requires a (C_x/C_o) 30 $\times$ smaller than required for the 3% bandwidth filters used in conventional band-select communication front-ends. In this respect, for RF channel-selection, Q is generally the more difficult of the two attributes to satisfy. Note that the needed Q is a function of frequency. In particular, a 1-MHz bandwidth is 0.1% at 1 GHz, for which a $Q > 10{,}000$ is desired for less than 2dB of insertion loss in a two-resonator filter; but at 433 MHz, it's 0.23%, for which a Q around 4,000 would be sufficient.

Up till now, no sputtered thin-film piezoelectric resonator operated at room temperature published so far possesses sufficient Q to realize a 0.1% bandwidth RF channel-select filter with insertion loss commensurate with the needs of wireless front-ends. Capacitive-gap transduced resonators, on the other hand, do possess sufficient Q at the needed frequencies, with Q's greater than 40,000 already demonstrated at 3 GHz by polydiamond ring resonators [6]. Unfortunately, capacitive-gap resonators suffer in the transducer coupling department, as the (C_x/C_o)'s so far demonstrated at GHz frequencies are far short of the requirement when a tuning inductor is not available to remove shunt capacitance C_o, as was done in [7].

To achieve simultaneous high Q and strong (C_x/C_o), either the (C_x/C_o)'s of capacitive-gap transduced resonators must be enhanced, or the Q's of piezoelectric resonators must be raised. The former approach is presently being explored by shrinking electrode-to-resonator gap spacings, such as done in [8] and [9]. So far, there has been some success at 60-MHz, at which a wine-glass disk resonator using partial-filled ALD gaps with spacings equivalent to 37.6 nm achieved

Manuscript received December 22, 2013; revised June 17, 2014; accepted June 19, 2014. Date of publication July 16, 2014; date of current version March 31, 2015. This work was supported by the Defense Advanced Research Projects Agency (DARPA) Chip-Scale-Spectrum Analyzers Program. Subject Editor G. Piazza.

L.-W. Hung was with the Department of Electrical and Engineering Computer Sciences, University of California at Berkeley, Berkeley, CA 94720 USA. She is now with IBM T. J. Watson, Yorktown Heights, NY 10598 USA (e-mail: lhung@us.ibm.com).

C. T.-C. Nguyen is with the Department of Electrical Engineering and Computer Sciences, University of California at Berkeley, Berkeley, CA 94720 USA (e-mail: ctnguyen@eecs.berkeley.edu).

Color versions of one or more of the figures in this paper are available online at http://ieeexplore.ieee.org.

Digital Object Identifier 10.1109/JMEMS.2014.2332991

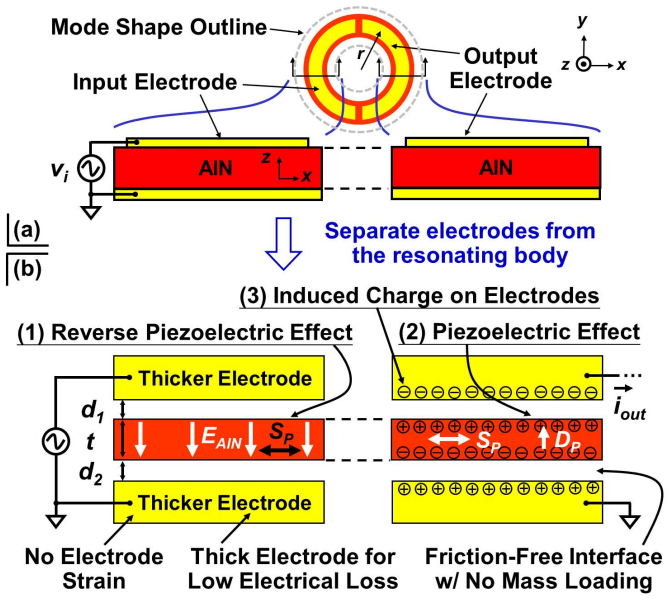

Fig. 1. (a) Conventional piezoelectric transducers employing electrodes that directly contact the piezoelectric resonator structure (*i.e.*, AlN film); and (b) working principal of a capacitive-piezo resonator for which electrodes are separated from the piezoelectric structure via tiny air gaps.

a simultaneous Q of 73,000 and motional resistance of 130 Ω, with a (C_x/C_o) of 0.39% [9]. However, similar Q and (C_x/C_o) marks are yet to be demonstrated at GHz frequencies, where shrinking resonator sizes reduce the total coupling afforded by capacitive-gap transducers, making it more difficult to achieve sufficiently large (C_x/C_o).

On the micro-scale piezoelectric side, some of the more successful efforts to raise Q borrow from HBAR technology, employing more complicated fabrication processes to combine readily micromachinable piezoelectrics, like aluminum nitride (AlN), with higher Q materials, like sapphire [10], silicon carbide [11], [12] or quartz [13], to achieve overall higher Q by either operating in overtone modes; or retaining traditional contour or lamb-wave modes and benefitting from an energy-sharing based Q-boosting, much like that of [14], to achieve Q's as high as 5,510 at 2.9 GHz [11], [15]. Values like this, however, are still short of the 30,000 needed for RF channel-selection at this frequency. They also come at the price of smaller (C_x/C_o), and for the case of HBAR's and LOBAR's, multiple modes, many of which must be removed by a second wider-band filter that inevitably adds cost and insertion loss.

Thus, non-overmoded AlN-only realizations are still of great interest. For AlN-only resonators, efforts to raise Q while retaining sufficient (C_x/C_o) have included careful anchor design and electrode engineering, where electrodes attached to the piezoelectric resonator structure have been thinned and patterned to reduce loading as much as possible. The use of alternative electrode materials has also been explored [16], as has altering resonator geometry [17]. Although these methods do increase mechanical Q, they still suffer from interface losses, and the increased resistance in thinned electrodes also decreases electrical Q. So far, demonstrated Qs are still less than 4,000 [16], [17].

Pursuant to increasing the Q of piezoelectric resonators without the need for multiple resonator materials or overmoding, this work borrows from work on BVA resonators in the 1970's [18] and simply separates piezoelectric contour-mode AlN resonators from their electrodes by tiny submicron gaps, as shown in Fig. 1, which compares the new device in (b) with a conventional version in (a). In doing so, the resulting capacitive-piezoelectric (or "capacitive-piezo") transducer eliminates metal material and metal-to-piezoelectric interface losses thought to limit thin-film piezoelectric resonator Q, while also maintaining high electric field strength through the piezoelectric material to preserve a strong piezoelectric effect. In essence, this capacitive-piezo transducer merges the strengths of capacitive and piezoelectric mechanisms to achieve a combination of electromechanical coupling and Q higher than otherwise attainable by either mechanism separately.

In addition, this capacitive-piezo transducer concept does not require dc-bias voltages and allows for much thicker electrodes that reduce series resistance without mass loading the resonant structure. The latter is especially important as resonators and their supports continue to scale towards even higher frequencies. In this work, use of capacitive-piezo transducers yields a 1.2-GHz contour-mode AlN ring resonator with a motional resistance of 889 Ω and a Q =3,073 [19] on par with the best among other reported d_{31}-transduced non-overmoded AlN-only piezoelectric resonators at this frequency [16], [17]. Moreover, a 50-MHz disk array posts an even higher Q =12,748 [20], which is presently the highest reported among sputtered AlN-only resonators, albeit at VHF.

After presenting the logic and mechanism behind this approach in Sections II-III, Sections IV-V then detail an analytical model for this capacitive-piezo transduced device and compare it to that of conventional piezoelectric devices. Section VI then presents the complete fabrication process flow used to achieve actual devices, and Section VII finally summarizes experimentally measured results verifying the performance enhancements afforded by this method.

II. Metal Electrode-Induced Degradation

As mentioned, polysilicon resonators routinely achieve the Q > 10,000 needed for RF channel-selection and frequency gating spectrum analyzers, but do so with higher than-desired impedances. To date, the measured Q's of polysilicon resonators are on the order of 20 times larger than that of sputtered AlN resonators with attached electrodes at similar frequencies. Interestingly, this defies the expectation of material loss theory [21]–[23], which predicts that the phonon-phonon interaction-constrained $f \cdot Q$ product of AlN material should only be about two times lower than that of silicon, with a theoretically expected Q on the order of 25,000 at 1 GHz [24]. Indeed, while measured Q's for polysilicon (*e.g.*, $Q = 161,000$ at 61.9 MHz [25]) or single-crystal silicon (*e.g.*, $Q = 77,000$ at 85.9MHz [26]) resonators have approached theoretical prediction, those for attached-electrode AlN resonators demonstrated so far fall far behind it. This large deviation is unlikely due to the difference between material

properties of single-crystal AlN used for theory and sputtered AlN used in measurement, given the fact that the measured Q of a thickness-mode FBAR constructed of epitaxial single-crystal AlN deposited at 1200–1300 °C via MOCVD (Metal Organic Chemical Vapor Deposition) on a SiC wafer [27] is essentially the same $Q\sim$1,000 as measured for FBARs constructed of sputtered AlN.

Results like this suggest that sputtered AlN material itself might not be the principal culprit among Q-limiting losses, but rather the metal electrodes or the electrode-to-resonator interface strain might be more responsible [28]. In fact, experimental data shows that as the thickness of a piezoelectric resonator's electrode increases, both the resonance frequency and Q of the resonator drop due to mass loading and electrode loss, respectively [29]. Electrode-derived energy loss perhaps also contributes to the lower Q's measured for d_{31}-transduced AlN resonators, where electrodes often cover maximum-strain locations, versus those for d_{33}-transduced thickness-mode resonators, for which electrodes are placed very close to the anti-nodes of the acoustic standing waves. Despite their lower Q's, d_{31}-transduced resonators are arguably more attractive than d_{33}, since their frequencies are set by CAD-definable lateral dimensions, so are more suitable for on-chip integration of multiple frequencies.

Whether a resonator uses d_{31} or d_{33}, both share the common problem that Q degrades as dimensions scale to achieve larger coupling and/or higher frequencies. In particular, while a piezoelectric structure can be scaled down, its electrode thickness often cannot scale as aggressively, since doing so increases electrical loss derived from increased electrode and interconnect electrical resistance.

Plenty of researchers have recognized the adverse effects of metal electrodes on the Q's of attached-electrode thin-film piezoelectric resonators and have sought to remedy this problem via a variety of approaches that span from reducing electrode roughness [30], to optimizing the electrode material [16], [31], to carefully balancing the AlN-to-electrode thickness ratio [32], to use of Bragg reflection to prevent energy loss [33]. Unfortunately, none of the above methods raises the Q's of on-chip piezoelectric resonators to the values needed for RF channel-selection and frequency gating spectrum analysis.

If the metal is the problem, then one plausible solution is to just remove the metal, or at least remove losses associated with the metal-to-piezoelectric interface. With this in mind, the researchers of [34] used undoped single-crystal AlGaAs deposited via MOCVD at 580 °C as the piezoelectric resonator material and AlGaAs doped with Si (AlGaAs:Si) for its electrodes, not only replacing the metals conventionally used in piezoelectric resonators, but essentially eliminating material differences at the resonator-to-electrode interface, thereby eliminating the associated interface losses. All of this led to a demonstrated Q of 25,390 at 21.77 MHz, much higher than those typically exhibited by piezoelectric contour mode resonators with attached electrodes in this frequency range. However, there is some question of whether or not such a Q can be retained at much higher UHF frequencies. In particular, at GHz RF frequencies, the need to minimize support loss dictates very small support cross-sections, which in turn mandates small interconnect cross-sections, raising the electrical resistance in series with the device. This increased series resistance can then load the Q of the resonator system, setting a Q ceiling that depends heavily on the conductivity of the interconnect material. This is where the use of a semiconductor material for conductive leads rather than metal can compromise performance.

In the end, metal interconnect is still much preferred, and a solution to the above that mitigates the mechanical Q losses of metal interconnects while retaining their high electrical conductivity is most desirable.

III. The Capacitive-Piezo Transducer

From the above discussion, it seems that Q degradation is difficult to avoid as long as the electrode is in physical contact with the piezoelectric structure (which generates loss through strain coupling) and as long as the piezoelectric structure governs the size and thickness of the electrode (which governs electrical loss). Interestingly, all of these issues can be circumvented by mechanically decoupling the electrodes from the resonating body, i.e., by simply separating the electrodes from the vibrating structure so that they are no longer in contact, as shown in Fig. 1(b). The resulting capacitive-piezo transducer should not only raise the Q of the piezoelectric film, but should also allow much thicker (hence much less resistive) electrodes without the electrode mechanical loss and mass loading penalties that would otherwise result if the electrode makes contact Of course, the smaller series resistance of thicker electrodes should also further increase the Q.

The working principal of this capacitive-piezo transducer is similar to that of a conventional piezoelectric resonator:

1) At the input port, voltage applied across two electrodes generates an electric field across the piezoelectric resonator that induces mechanical strain via the reverse-piezoelectric effect.
2) If the frequency of the input voltage equals that of a mode, the resonator structure begins to vibrate with significant amplitude at both its input and output ports, generating mechanical strain at both locations.
3) At the output port, the mechanical strain induces electrical displacement current D_z via the piezoelectric effect.
4) The equivalent bonded surface charges on the piezoelectric surfaces in turn induce charges of opposite sign on the electrodes across the gap.

As mentioned, although not a well-known technique, the use of contactless electrodes on piezoelectric resonators is not new, having been demonstrated on 5- and 10-MHz macroscopic quartz crystal resonators, called BVA resonators, as far back as 1976 [18]. Since the piezoelectric-to-electrode thickness ratio of these devices was on the order of 100μm-to-100nm, or 1000, separating the electrode from the piezoelectric did little to increase the Q of the device. It did, however, allow for a more stable device against drift, since it eliminates electrode-to-resonator stress variations over time [35]. This was the main reason for investigating such devices in the past.

For the present micromechanical resonators, on the other hand, the piezo-electric-to-electrode thickness ratio is much

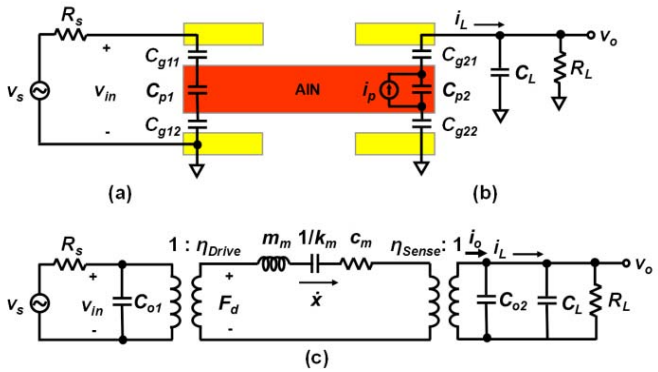

Fig. 2. Equivalent electrical circuit at (a) input and (b) output, modeling the effect of electrode-to-resonator gap spacing on the electromechanical coupling coefficient. (c) Same circuit but with the capacitive-piezo resonator replaced by its transformer-based equivalent electrical circuit.

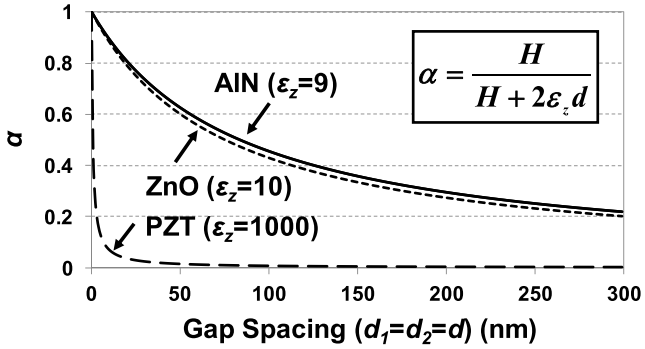

Fig. 3. Plot of α versus capacitive-piezo electrode-to-resonator gap spacing (on each side) according to (4) for three common piezoelectric materials. Here, the induced electric field within a piezoelectric film decreases by a factor of α when air gaps d_1 and d_2 are introduced between the electrodes and the resonator structure. The equivalent electromechanical coupling coefficients and static capacitance over both input and output ports are linear functions of α, and therefore functions of gap spacing.

smaller, on the order of 10. Thus, the case for using a capacitive-piezo transducer to increase Q is much stronger on the micro-scale. In addition, the ease with which small electrode-to-resonator gaps can be achieved via MEMS technologies further encourages the use of contactless electrodes. In effect, capacitive-piezo transducers stand to improve the Q and drift stability of micro-scale thin-film piezoelectric resonators, while maintaining fabrication cost only slightly higher than the already low cost of capacitive-gap transduced resonators that presently dominate the MEMS timing industry.

IV. Transducer Modeling

Equivalent electrical circuit models for conventional AlN contour-mode resonators with contacting electrodes, such as described in [36], are abundant in the literature. In particular, values for the *LCR* circuit based on actual values of dynamic mass, stiffness, and damping, with location-dependent formulations, are well covered [36]. Thus, the focus of the present approach to modeling the capacitive-piezo resonator is on how its electrode-to-resonator air gaps influence the electromechanical coupling coefficients that gauge transducer efficiency at the drive and sense ports.

A. Drive Electromechanical Coupling

The electromechanical coupling coefficient at the input (or drive) port, indicated in Fig. 2(c), is defined as

$$\eta_{Drive} = \frac{F(j\omega)}{V_{in}(j\omega)} \tag{1}$$

where $F(j\omega)$ is the force generated in the piezoelectric material and $V_{in}(j\omega)$ is the input voltage across the top and bottom electrodes. Here, a sinusoidal input is assumed throughout this analysis. η_{Drive} models how efficiently the electrical domain voltage input is transduced into a mechanical domain force that drives the piezoelectric layer into resonance vibration.

Under normal operation, a voltage applied across the top and bottom electrodes induces a z-directed electric field that in turn generates an r-directed mechanical strain S_r and associated stress T_r on the AlN film via the reverse piezoelectric effect. The magnitude of induced stress T_r equals the product of the piezoelectric stress constant e_{31} ($e_{31} \sim 0.7$ C/m^2 for sputtered AlN) [36] and the electric field established within the AlN film ξ_{AlN}, or

$$T_r = e_{31}\xi_{AlN} \tag{2}$$

The gap-AlN-gap stack essentially comprises three capacitors in series, as shown in Fig. 2(a), for which ξ_{AlN} takes the form

$$\xi_{AlN} = \frac{v_{in}}{H + \varepsilon_z d_{Total}} = \frac{v_{in}}{H} \cdot \alpha = \xi_{AlN, d_{Total}=0} \cdot \alpha \tag{3}$$

where ε_z ($\sim$9) is the relative permittivity along the c-axis of the AlN material; H is its thickness; d_{Total} is the total air-gap spacing between the electrodes ($d_{Total} = d_1 + d_2$); and (as will be seen) α is a function gauging the degree to which the coupling coefficient degrades with increasing air gap spacing:

$$\alpha = \frac{H}{H + \varepsilon_z d_{Total}} \tag{4}$$

From (4), α is less than unity, and $\alpha = 1$ for conventional attached-electrode AlN resonators, for which $d_{Total} = 0$. Fig. 3 plots α against gap spacing d (assumed the same on both sides) for a 1.5μm-thick resonator structure in various piezoelectric materials. To maximize the electric field in the AlN, α must be maximized, which calls for either small gaps or a piezoelectric material with low permittivity.

When the frequency of the input voltage matches one of the structure's mode frequencies, the lateral force associated with the induced stress T_r excites the resonator into lateral-mode vibration in the associated mode shape. The dashed lines in Fig. 1(a) depict the intended high frequency second radial-contour mode shape targeted in this work, in which the inner and outer edges of the ring contract and expand, respectively, in a motion reminiscent of breathing, much like the device of [37]. Note that for this particular mode shape, there is ideally no strain, stress, or displacement associated with the angular component.

The resulting modal force can be written as the product of the induced stress T_r, the cross-sectional area normal to

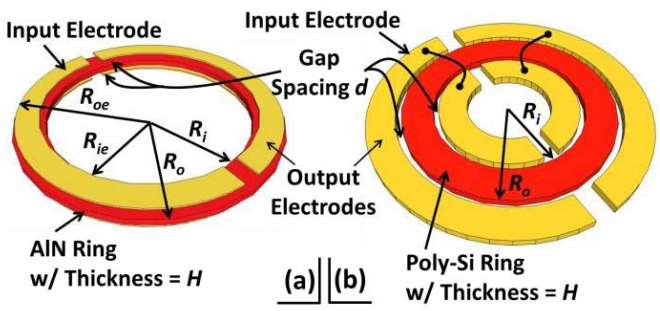

Fig. 4. Electrode arrangements for (a) the capacitive-piezo AlN ring resonator and (b) the capacitive-gap poly-Si ring resonator discussed in the text and to be compared in Fig. 7. Both devices operate in the same radial mode shape at 1.2GHz.

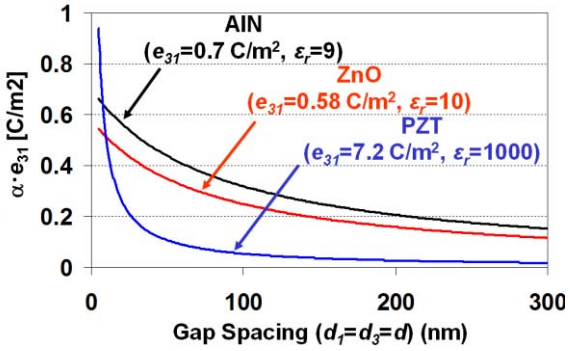

Fig. 5. Simulated plot of the effective $\alpha \cdot e_{31}$ versus electrode-to-resonator gap spacing, showing a clear decrease with increasing gap spacing. The gap spacing affects the coupling of PZT the most due to its much larger relative permittivity ε_r.

the stress ($Hr \cdot d\theta$), and the normalized mode shape $\Phi(r)$, integrated over the electrode coverage area:

$$F = \int_0^{\pi} \int_{R_{ie}}^{R_{oe}} T_r (Hr \cdot d\theta)\Phi(r)dr = (\pi) \cdot (T_r H) \cdot \int_{R_{ie}}^{R_{oe}} r\Phi(r)dr \quad (5)$$

where R_{ie}, and R_{oe} are the inner and outer radius of the electrode, respectively, as indicated in Fig. 4(a), and $\Phi(r)$ is the normalized mode shape, given by

$$\Phi(r) = \frac{\varphi(r)}{\int_{R_{ie}}^{R_{oe}} \varphi(R_r)dr} \quad (6)$$

where $\varphi(r)$ is the mode shape of a ring vibrating in its 2nd contour mode (anti-symmetric mode), normalized to the maximum value (i.e. $\varphi(r) <= 1$ for any r in the domain and $\varphi(r) = 1$ at the largest displacement point).

Using (2)-(4), the distributed stress T_r takes the form

$$T_r = E_P S_r = e_{31} E_{AlN} = e_{31} \left(\frac{V_{in}}{H} \cdot \alpha \right) \quad (7)$$

where E_P is the Young's modulus of the resonator material, and V_{in} is the amplitude of the sinusoidal input.

Plugging (7) into (5) and further into (1), yields for the modal force F and η_{Drive}, respectively:

$$F = \alpha \cdot e_{31} \cdot V_{in} \cdot \pi \int_{R_{ie}}^{R_{oe}} r\Phi(r)dr \quad (8)$$

$$\eta_{Drive} = \alpha \cdot e_{31} \cdot \pi \int_{R_{ie}}^{R_{oe}} r\Phi(r)dr \quad (9)$$

From (9), η_{Drive} is proportional to both e_{31} and α, the latter of which is in turn a function of the permittivity ε_z. Thus, piezoelectric materials with simultaneous high e_{31} and low permittivity are most suitable when attempting to maximize the electromechanical coupling coefficient of a capacitive-piezo transduced device. For comparison, Fig. 5 plots the ($\alpha \cdot e_{31}$) product against total gap spacing d_{Total} for various piezoelectric materials. As expected, small gap spacing is preferred to maintain a high coupling coefficient. On the other hand, note that a large e_{31} does not guarantee a large coupling coefficient. As shown in Fig. 5, even though PZT has a larger e_{31} than AlN and ZnO, its capacitive-piezo coupling is weaker at most gap spacings due to its much higher relative permittivity.

The electrode geometry and configuration affects η_{Drive} via the last term in (9). Given the same electrode area and static capacitance, the coupling coefficient η_{Drive} is maximized by placing electrodes over locations that experience maximum strain. In a conventional piezoelectric resonator with contacting electrodes, this degrades the Q, since it dissipates more energy via larger strain at the electrode/resonator interface and larger strain coupled to the electrodes. Clearly, the non-contacting electrodes of a capacitive-piezo transducer obviate this problem, providing a major advantage.

B. Sense Electromechanical Coupling

The equivalent circuit of Fig. 2 converts the (across variable) force generated by the electric field at the input port to a (through variable) velocity via the series *LCR* circuit taking on values of mass m_m, compliance ($1/k_m$), and damping c_m, with expressions for element values provided in previous literature [38]. The ensuing displacement (velocity) is then converted to charge (current) by the electromechanical coupling coefficient at the output (or sense) port, indicated in Fig. 2(c), which takes the form

$$\eta_{Sense} = \frac{Q_P(j\omega)}{U(j\omega)} = \frac{\int_A D_z dA}{U(j\omega)} \quad (10)$$

where Q_P is the total charge induced via the piezoelectric effect at the output port, equal to the displacement current (charge/area) D_z integrated over the electrode area; and $U(j\omega)$ is the maximum displacement amplitude. η_{Sense} models how efficiently the mechanical domain velocity transduces into an electrical domain output current.

Since the *LCR* is a resonant circuit, appreciable velocity results only when the input drive signal is at or near resonance. Once resonance vibration ensues, symmetry of the second contour mode shape mimics the drive-side velocity profile at the sense side, thereby duplicating the strain. The sense side strain then polarizes the AlN film via the piezoelectric effect.

Assuming only radial mechanical displacement, the resulting electric displacement (charge per area) takes the form

$$D_z = e_{31} S_{r,Sense} = e_{31}\left[\frac{\partial u_r}{\partial r} + \frac{u_r}{r}\right] \tag{11}$$

where $u_r(r, j\omega)$ is the time-varying radial mechanical displacement as a function of position r. $u_r(r, j\omega)$ can be decomposed into the product of a time-varying function $U(j\omega)$ and the stationary mode shape $\phi(r)$

$$u_r(r, j\omega) = U(j\omega)\phi(r) \tag{12}$$

Integration of D_z over the electrode area yields the total induced charge, Q_P

$$\begin{aligned} Q_P &= \int_0^{\pi}\int_{Rie}^{Roe} D_z r\,dr\,d\theta \\ &= \pi e_{31} U(j\omega) \int_{Rie}^{Roe}\left(r\frac{\partial\phi(r)}{\partial r} + \phi(r)\right)dr \end{aligned} \tag{13}$$

Plugging (13) into (10) finally yields the expression for η_{Sense} for the case where there is no gap between the piezoelectric resonator and its electrodes:

$$\eta_{Sense,NoGap} = \pi e_{31} \int_{Rie}^{Roe}\left(r\frac{\partial\phi(r)}{\partial r} + \phi(r)\right)dr \tag{14}$$

Correct modeling of the actual current delivered to the output when electrodes are separated from the piezoelectric requires that the impedance of the gaps be included. To this end, the output is first modeled by a current source, as shown in Fig. 2(b), where output current i_p is merely the time derivative of Q_P, or $i_p = \omega Q_P$. Taking the ideal case where the load impedance $(R_L \| (1/(sC_L))$ is zero, i.e., the output is grounded, yields for output current:

$$i_o = i_p \cdot \frac{Z_{p2}}{Z_{p2}+Z_{g21}+Z_{g22}} \approx i_P \cdot \frac{H}{H+\varepsilon_z(d_{21}+d_{22})} = i_p \cdot \alpha \tag{15}$$

where Z_{p2}, Z_{g21}, and Z_{g22} are the static piezoelectric material and gap impedances, respectively, associated with the capacitors in Fig. 2(b). As shown, gaps modify the effective output current by the now familiar factor α, yielding an effective coupling factor given by

$$\eta_{Sense} = \alpha \cdot e_{31} \cdot \pi \int_{R_{ie}}^{R_{oe}}\left(r\frac{\partial\phi(r)}{\partial r} + \phi(r)\right)dr \tag{16}$$

where η_{Sense} is shown in Fig. 2(c) with C_{o2} equal to the series combination of C_{p2}, C_{g21}, and C_{g22}.

Similar to η_{Drive}, η_{Sense} is proportional to e_{31} and α. From the equivalent circuit, the input port-to-output port motional resistance of the resonator can therefore be determined according to

$$R_m = \frac{c_m}{\eta_{Sense}\eta_{Drive}} \tag{17}$$

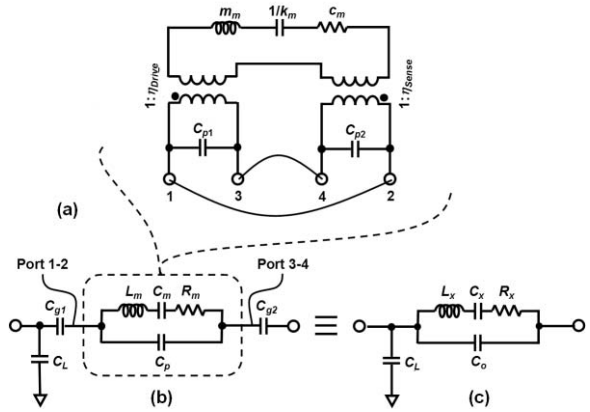

Fig. 6. Equivalent circuit transformations used to study the effect of electrode-to-resonator gaps on the series and parallel resonance frequencies and on the equivalent coupling coefficient. (a) Four-terminal model of a conventional two-port piezoelectric resonator (with no air gaps) under a one-port measurement scheme, with terminals 1-2 connected and 3-4 connected. (b) BVD model of (a), enclosed by the dash lines, with two series capacitors, C_{g1} and C_{g2}, representing air gaps inserted into both input and output ports of the resonator. (c) Equivalent BVD model of (b) with C_{g1} and C_{g2} lumped into the resonator branch.

where c_m is the mechanical damping, defined as

$$c_m = \frac{\omega_o m_m}{Q} \tag{18}$$

where ω_o is the radian resonance frequency, and m_m the effective mass representing the inductor value in Fig. 2(c).

From (9) and (16), the drive and sense coupling coefficients for a capacitive-piezo resonator are smaller by a factor α than those of an equivalently-sized conventional piezoelectric device using contacting electrodes. However, this does not necessarily mean that its port-to-port motional resistance is smaller. In fact, according to (17) and (18), it is possible for the motional resistance of a capacitive-piezo transduced device to be lower than that of a conventional counterpart with contacting electrodes if the reduction in loss provided by electrode separation raises its Q over the conventional device by a factor larger than α^2.

V. Motional-to-Static Capacitance Ratio

As mentioned in Section I, the motional-to-static capacitance ratio (C_x/C_o) provides a measure of the maximum distortion-free filter bandwidth achievable by resonators using a given input/output (I/O) transducer type. Perhaps the simplest way to determine this ratio for the capacitive-piezo transducer is to first generate a classic Butterworth Van Dyke (BVD) equivalent circuit modeling the impedance of a single one of its ports, with all other ports grounded, using the transformations shown in Fig. 6. Here, two capacitors, C_{g1} $(= C_{g11} + C_{g21})$ and $C_{g2}(= C_{g12} + C_{g22})$, model the air-gaps in series with the input/output ports, *cf.* Fig. 2; and the capacitor C_p $(= C_{p1} + C_{p2})$ in shunt with the motional *LCR* models the static capacitance of the piezoelectric structure. C_{g1} and C_{g2} can be absorbed into the resonator branches to form an equivalent circuit, shown in Fig. 6(c), with modified

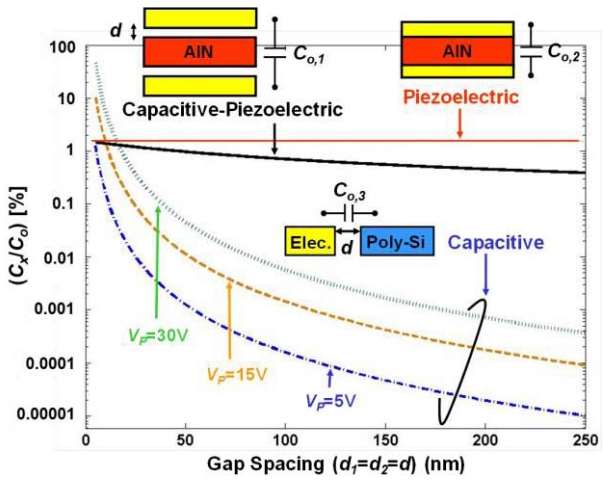

Fig. 7. Comparison of (C_x/C_o) of capacitive-gap with V_P of 5V to 30V, piezoelectric, and capacitive-piezo transducers as a function of gap spacing, all for 1.2-GHz designs. Capacitive-piezo transducers equipped with small gaps maintain high (C_x/C_o), although lower than piezoelectric ones, with both orders of magnitude higher than that of capacitive-gap transducers with gaps greater than 30nm. At V_P =30V, the capacitive-gap transducer attains larger (C_x/C_o) than the piezoelectric ones when its gap is scaled below 17nm.

component values

$$L_x = L_m \cdot \left(\frac{C_g + C_p}{C_g}\right)^2 = L_m \cdot \alpha^{-2} \tag{19}$$

$$C_x = C_m \cdot \left(\frac{C_g^2}{(C_g + C_p)(C_g + C_p + C_m)}\right) = C_m \cdot \frac{(C_g + C_p)}{(C_g + C_p + C_m)} \cdot \alpha^2 \tag{20}$$

$$R_x = R_m \cdot \left(\frac{C_g + C_p}{C_g}\right)^2 = R_m \cdot \alpha^{-2} \tag{21}$$

where C_g is the total capacitance contributed by the air gaps on both sides:

$$C_g = \left(C_{g1} \cdot C_{g2}\right) / \left(C_{g1} + C_{g2}\right) = C_{g1} \,\|\, C_{g2} \tag{22}$$

and where the fact that $C_g/(C_g + C_p) = \alpha$ has been used. From (21), the addition of air gaps increases the motional resistance by α^{-2}. This matches (17) with the recognition that the equivalent electromechanical coupling coefficients at both input and output ports each include degradation ratios equal to α.

Since the effective static capacitance at the port is given by

$$C_o = \left(C_p \cdot C_g\right) / \left(C_p + C_g\right) = C_p || C_g \tag{23}$$

the motional-to-static capacitance ratio becomes

$$\frac{C_x}{C_o} = \frac{C_m}{C_p} \cdot \frac{C_g}{C_g + C_p + C_m} \approx \frac{C_m}{C_p} \cdot \alpha \tag{24}$$

where the last form holds for the usual case when $C_m \ll C_p$. As expected, (C_x/C_o) approaches the conventional (i.e., contacting electrodes) value of (C_m/C_p) when $C_g \gg (C_p + C_m)$, i.e., when the gap spacing is very small.

Fig. 7 compares simulated plots of (C_x/C_o) versus gap spacing d for 1.2-GHz ring resonators using three different transducer types: piezoelectric, capacitive-piezo, and capacitive-gap alone. The simulations employ AlN rings for the d_{31} piezoelectric-based transducers, and a polysilicon ring for the capacitive-gap transduced one, shown in Fig. 4(b). Each ring, regardless of material, has an inner radius and thickness of 25.6μm and 1.5μm, respectively; but differing ring widths of 5μm for AlN and 4.3μm for polysilicon, both chosen to achieve a 1.2-GHz resonance frequency using the same 2nd radial-contour mode shape, neglecting the effects of DC bias-induced electrical spring softening inherent to capacitive-gap transduced resonators. In addition, the electrodes for the polysilicon resonator are assumed to be placed both inside and outside the ring, similar to [37]. As expected, the (C_x/C_o) of the capacitive-piezo transducer depends on gap spacing, but not as strongly as one might think, mainly because C_o drops by the same ratio α as the electromechanical coupling coefficients when the gap spacing increases. Even so, a capacitive-piezo transducer with a 200 nm gap spacing achieves a (C_x/C_o) of 0.4%, for which a capacitive-gap (alone) transducer with dc bias of 15V (V_P = 15V) would require a much smaller gap spacing of 16 nm. This relaxed gap spacing constitutes a distinct advantage of capacitive-piezo transducers over capacitive-gap ones.

It should be noted that if gap spacing had no limit, the capacitive-gap transducer can actually outperform all others, with a (C_x/C_o) that bests even the conventional piezoelectric device when the gap is scaled below 17nm with V_P = 30V. For practical applications, however, the utility of this approach must be weighed against any yield loss resulting from the use of such a small gap.

A. k_{eff}^2 and Effect of Load Capacitance C_L

Although a capacitive-piezo resonator's (C_x/C_o) does get worse as its electrode-to-resonator gap increases, the degradation rate is tempered by the fact that C_o also decreases alongside C_x, albeit more slowly. This, however, is the case only if the device capacitance dominates over the shunt load (i.e., parasitic) capacitance C_L from interconnects and bond pads, shown in Fig. 2. Since C_o will be smaller than the original C_p of the device, it will be much less likely that it will dominate over C_L, so a formulation that includes the effect of C_L is of interest.

Since practical ladder filter design using electrically coupled piezoelectric resonators often entails superimposing the series and parallel resonances of resonators used in the ladder, a useful way to gauge the electromechanical coupling of a given resonator is via the separation between its series and parallel resonances. Here, larger separation indicates stronger coupling. Since the introduction of air gap capacitors in series with the static piezoelectric material capacitance normally reduces coupling, it should also reduce the separation between series and parallel resonance frequencies.

To quantify this, use of Fig. 6(b) in the circuit of Fig. 1(b) yields for the series resonance frequency of the device

$$f_s = \frac{1}{2\pi}\sqrt{\frac{1}{L_x C_x}} = \frac{1}{2\pi}\sqrt{\frac{1 + \frac{C_m}{C_p + C_g}}{L_m C_m}}$$

$$= f_{nom} \cdot \sqrt{1 + \frac{C_m}{C_p + C_g}} \tag{25}$$

where

$$f_{nom} = \frac{1}{2\pi}\sqrt{\frac{1}{L_m C_m}} \tag{26}$$

Note that (25) increases as the air gap spacings increase. This upward frequency shift derives from the reactance change introduced by the air gaps [39] and should not be confused with the upward frequency shift caused by elimination of electrode mass loading when electrodes are separated from the piezoelectric material. When considering the parallel resonance frequency, the air-gap capacitor C_g is essentially in series with the load capacitance C_L. Given this, the parallel resonance frequency takes the form

$$f_p = \frac{1}{2\pi}\sqrt{\frac{1+\frac{C_m}{C_p+C_g||C_L}}{L_m C_m}} = f_{nom} \cdot \sqrt{1+\frac{C_m}{C_p + C_g||C_L}} \tag{27}$$

which also increases with increasing air gap spacing, but not as fast as (25). Thus, the separation between the series and parallel resonance frequency decreases with increasing gap spacing.

With expressions for the series and parallel resonance frequencies, the electromechanical coupling factor k^2_{eff} can be found. In particular, the most recent IEEE definition of k^2_{eff} is

$$k^2_{eff} = \frac{f_p^2 - f_s^2}{f_p^2} \tag{28}$$

Plugging (25) and (27) into (28) and rearranging yields

$$k^2_{eff} = k^2_{eff,d=0} \cdot \frac{C_g}{C_g+C_p} \cdot \frac{C_g}{C_g+C_L} \cdot \frac{C_p+C_m}{C_p+C_g||C_L+C_m} \tag{29}$$

where $k^2_{eff,d=0}$ is the effective electromechanical coupling coefficient when electrodes are attached to the piezoelectric material, *i.e.*, without gaps, so with C_g equal to infinity. When the load capacitance C_L is minimized such that $C_L \ll C_g$, the last two terms in (29) become unity, and

$$k^2_{eff} = k^2_{eff,d=0} \cdot \frac{C_g}{C_g + C_p} = k^2_{eff,d=0} \cdot \alpha \tag{30}$$

From (29) and (30), it is desirable to minimize load capacitance to ensure the condition $C_L \ll C_g$ holds so that k^2_{eff} differs from $k^2_{eff,d=0}$ only by a factor α. However, this might be difficult to do if the resonator size is small. For cases where C_L is large and smaller gaps are not practical, arraying of devices, as done in [25] and [7], can effectively raise the value of C_g.

B. Coupling Versus Q Trade-Off

Whether or not $C_L \ll C_g$, introduction of capacitive-piezo transducers will most likely reduce the effective electromechanical coupling coefficient, essentially trading it for higher Q. The good news is that the trade is not one-to-one. Specifically, theoretical prediction sets the Q ceiling of AlN resonators ten to twenty times higher than measured on attached-electrode devices, while α is 0.45 for a gap size of 100 nm and can be increased to 0.625 with 50 nm gap spacing, as shown in Fig. 3. Note that losses associated with electrodes are eliminated regardless of whether the gap size is 100 nm, 50 nm, or smaller, as long as there is a gap. Thus, capacitive-piezo transducers are likely to raise the $(k^2_{eff} \cdot Q)$ product. Furthermore, very small gaps might actually enable higher coupling than attainable by an attached-electrode device when one considers that separating the metal from the piezoelectric eliminates strain sharing between metal and piezoelectric, allowing more strain in the piezoelectric, hence stronger coupling.

At the very least, use of the capacitive-piezo transducer allows a designer to trade electromechanical coupling for Q—a trade-off that can greatly widen the filter design space for a given technology. For example, small percent bandwidth filters that require high Q resonators generally do not require large coupling, i.e., the smaller the bandwidth, the higher the needed Q, but the more modest the needed electromechanical coupling. Thus, given that piezoelectric resonators generally possess ample coupling, but insufficient Q, even if a capacitive-piezo transducer only provides a trading of coupling for Q, this trade-off could be instrumental to making possible the tiny percent bandwidth filters needed for RF channel-selecting front-end filters and all their associated benefits [40].

VI. Fabrication

AlN resonators employing capacitive-piezo transducers were fabricated using the 5-mask, CMOS-temperature-compliant process summarized in Fig. 8, where each column corresponds to cross-sections along different portions of the coupled ring resonator array at the top of the figure. The process begins with blanket depositions of 250 nm silicon oxide and 200 nm silicon nitride over 6" high-resistance wafers to serve as isolation layers. A lift-off process then follows to delineate interconnect and bottom electrodes composed of subsequent 30 nm-thick Al and 60 nm-thick Ni evaporated films, to yield the cross-section in Fig. 8(a). The Ni layer will later serve first as an etch stop when removing sacrificial molybdenum in the stem anchor trenches; and second, as a seed layer for electroplating nickel stem anchor material through these very trenches. The lift-off process employs I-line photoresist atop lift-off resist 3A (LOR3A, MicroChem Corp., Newton, MA) [41], to realize fine Al/Ni features with smooth edges critical for good sputtered AlN quality. Fig. 9(a) shows the lift-off photoresist edge cross-section after metal evaporation and before lift-off, where the concave sidewall of the photoresist effectively separates the metal traces to remain and metals to be removed by photoresist removal. The rather thin interconnect and bottom electrodes reduce surface topography, which serves two purposes: it improves step coverage of the thin sacrificial Mo to be deposited next; and perhaps more importantly, it helps to avoid poor AlN quality near the edges of the bottom electrodes. If thicker electrodes are desired for lower interconnect resistance, planarization steps, e.g., using chemical mechanical polishing (CMP) can be incorporated.

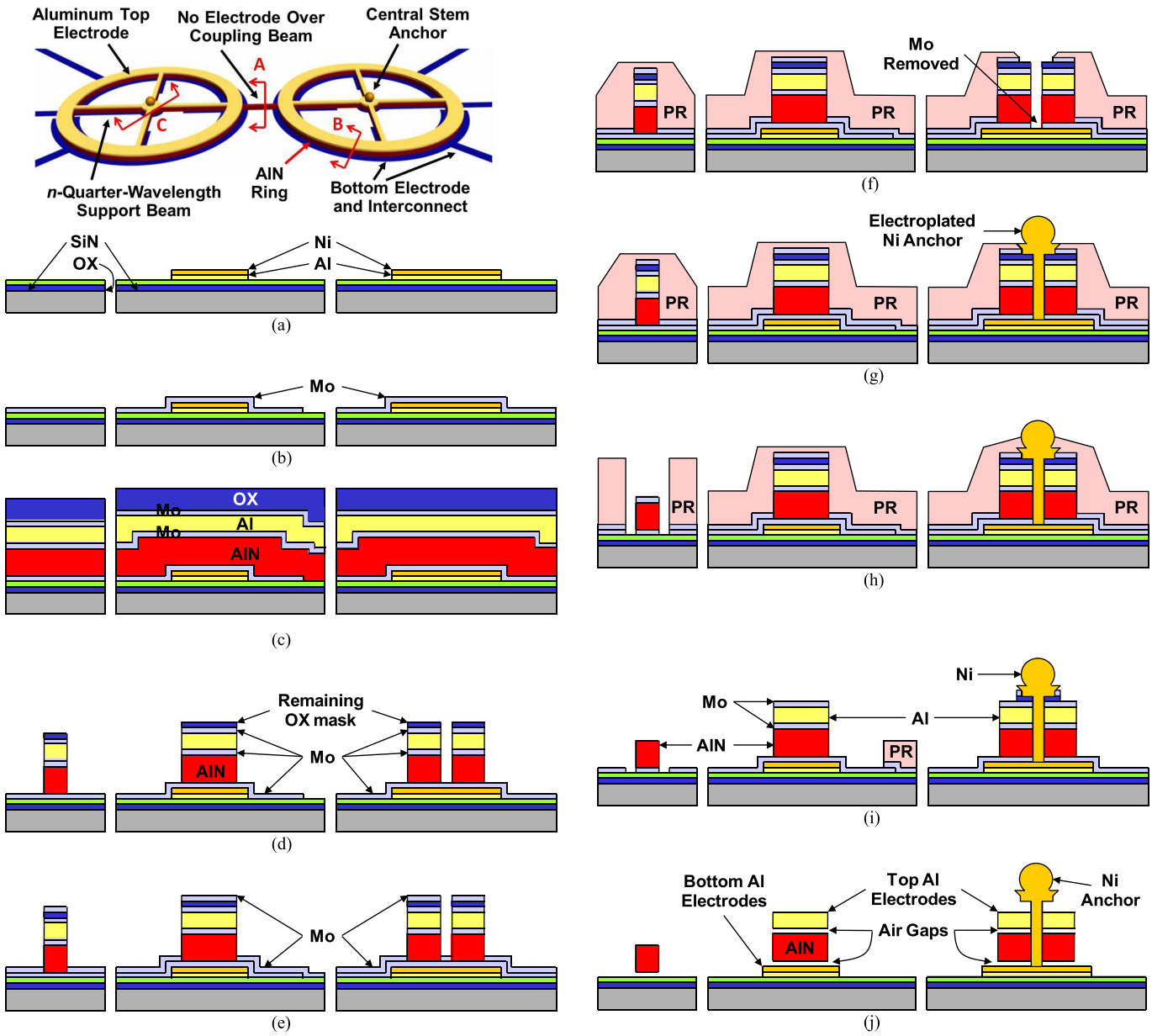

Fig. 8. Fabrication process flow for capacitive-piezo AlN resonators with electroplated Ni anchors and Mo sacrificial material dry released in XeF_2. Each column corresponds to one cross-section depicted in the top ring resonator array. Cross-section A: areas without top electrodes, such as coupling beam of resonator arrays and filters, and part of wine-glass disk resonators; cross-section B: areas with top electrodes; cross-section C: anchors. (continued on next column). (a) Deposit 250nm oxide and 200nm nitride on high resistive wafers as isolation layers, followed by lift-off patterning of 20nm Al/60nm Ni. (b) Sputter sacrificial Mo and pattern via wet etch. (c) Sputter the following films in sequence: AlN, Mo, Al, Mo, and PECVD oxide. (d) Pattern oxide as hard mask to dry etch Mo/Al/Mo/AlN. The etch stops on either the first sacrificial Mo layer or the nitride isolation layer. (e) Sputter 20 nm Mo to electrically connect the entire wafer for electroplating. (f) Etch away Mo within the anchor trenches to expose the underneath Ni layer as seed layer for electroplating. (g) Electroplate Ni from the bottom to fill the trenches, using Ni on the interconnect layer as seed layer. The top view of the anchor after this step can be seen in Fig. 10(a). (h) Pattern and remove thin Mo, the remaining oxide mask, and the top Al electrodes from the coupling beams and the areas of wine-glass disks without top electrodes. (i) Pattern PR to cover exposed nitride/oxide layers. Remove thin Mo layer and the remaining oxide layer on devices via dry etch. The etch stops on the barrier Mo layer or on AlN where the remaining oxide has been removed in the previous step. (j) Dry release devices in XeF_2/N_2 mixed gases; remove PR.

After bottom electrode formation, 250 nm Mo is then sputtered at 200 °C to serve as the sacrificial layer that defines the bottom electrode-to-resonator spacing. Sputtered Mo is used instead of more common sacrificial materials, such as oxide, silicon, or germanium, to attain better c-axis orientation of the sputtered AlN film. Here, a slight *in-situ* sputter etch via argon immediately before Mo sputtering seems to improve the orientation of the Mo surface plane to one more suitable for growth of the desired (002) AlN. The amount of pre-sputtering must be adjusted carefully, since excessive sputter etching can also roughen the surface enough to degrade AlN quality.

To further improve AlN quality, the Mo is patterned via a phosphoric acid/acetic acid/nitric acid-based wet etch into patches underlying each individual device, as shown in

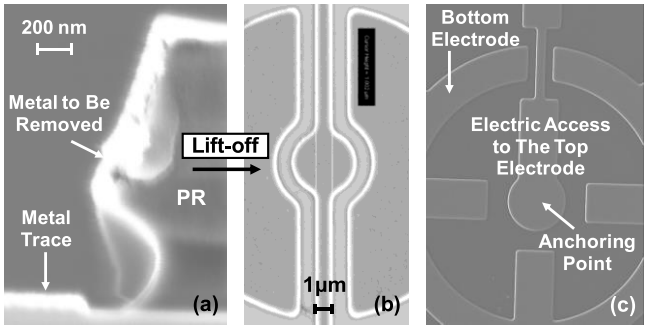

Fig. 9. (a) Cross sectional SEM showing the double-layer lift-off process that ensures smooth metal trace edges in (b). (c) Bottom electrode and interconnect configuration for a ring resonator, showing the "landing pad" for electrical contact to the eventual anchor at the very center.

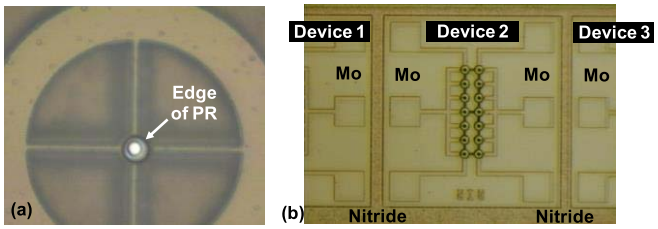

Fig. 10. (a) Optical photo of a 500-MHz ring resonator after step (g) in Fig. 8, showing the electroplated nickel anchor at the center with PR covering everything else. (b) Devices after step (h), showing the Mo patches patterned in step (b).

the overhead layout view of Fig. 10(b), where 5μm-wide streets devoid of Mo separate the Mo patches, *i.e.*, Mo still covers >99% of the entire wafer area. Such patterning helps to prevent excessive tensile stress (>500MPa) in reactively sputtered AlN, which tends to occur when it is sputtered directly over blanket Mo covering the entire wafer. When the Mo is patterned as in Fig. 10(b), AlN can be sputtered over it with low stress (< ±20MPa) and high FWHM (∼1.7°).

Before actual AlN deposition, several dummy runs in our university tool served to dial in the pressure and power of sputter deposition to insure a vertical strain gradient small enough to prevent bending of structures into electrodes. With proper dialing, bending-free AlN-only films were easier to attain than films with attached electrodes. A production tool dedicated to one process recipe would likely not require the dummy runs needed to dial-in the tool, here.

After sputtering the 1.5-μm AlN resonator structural material, several layers are sputtered in sequence: 250 nm Mo as a second sacrificial layer between the resonator and the top electrode, 400 nm Al as the top electrode, 20 nm Mo as a barrier layer between Al and the last layer, which is 1.2 μm PECVD oxide deposited at 300 °C to serve as an etch hard mask. At this point, the cross-section is as in Fig. 8(c). The 20nm of Mo between Al and oxide is essential for two reasons. First, it prevents Al from reacting with PECVD oxide during deposition. Second, it serves as an etch stop when removing the remaining oxide mask before release.

The oxide mask is then patterned to delineate suspended AlN structures (resonators and coupling links), top electrodes, and stem anchor openings, all at once. This is achieved via a CF_4/CHF_3 RIE etch that stops on the 20nm Mo barrier layer, followed by dry etch of the Mo/Al/Mo/AlN film stack without breaking vacuum, to yield the cross-sections of Fig. 8(d). The multi-layer etch process stops on the first Mo layer and on the nitride isolation layer in places where Mo was removed in the previous step.

Track (c) in Fig. 8 depicts formation of the all-important peg anchor used in this technology. Similar to the stems of [42], this peg comprises a hole filled with a strong (conductive) material that adheres well to both the substrate and to the sidewalls of the stem hole. Anchors of this type are superior to those formed by mere film deposition over vias [43], [44], since they are solid and make right angles to the structure at both the top and bottom edges. Thus, they present more ideal fully symmetric boundary conditions, which helps to minimize energy loss to the substrate through the anchors.

In contrast to the process of [42], where peg filling is achieved by depositing polysilicon (at a high temperature) using a 'top-down' LPCVD approach, the present process generates the peg at a much lower CMOS-compatible temperature by electroplating Ni into the peg hole opening, from the bottom-up. To prepare the wafer for electroplating, 20nm Mo is sputtered to electrically connect the whole wafer by connecting the individual Mo patches (Fig. 8(e)). This sputtering is performed at a lower chamber pressure (3 mTorr) to prevent sidewall coverage, which is necessary to ensure nickel is electroplated upward from the seed layer to fill the trench without voids. After patterning thick photoresist, Mo within the trenches is dry etched to expose Ni on interconnects (Fig. 8(f)) and the Ni anchor is electroplated from the underlying Ni seed layer using a solution of nickel sulfamate at 60 °C to yield the cross-section of Fig. 8(g) and optical photo of Fig. 10(a).

Another lithography and etch step is used to (1) remove oxide/Mo/Al from the coupling beams of any resonator array or filter in order to electrically isolate the input and output ports, and (2) to pattern the top electrode of some of the disk resonators to allow excitation of wine-glass modes. At this point, the cross-section is as in Fig. 8 (h).

After a simple lithography step to cover the exposed isolation oxide/nitride layers with photoresist, the thin Mo layer and the remaining oxide mask atop the structures are removed by dry etching (*cf.* Fig. 8(i)). This step, similar to the dry etch in step (d), requires that Mo and Al be dry etched one after the other, and this is done using Cl_2-based chemistries with varying amounts of added O_2 that alter etch selectivities.

The device is released by etching away all Mo using a XeF_2/N_2 mixed gas. After the sacrificial Mo is completely etched, both the top electrode and the AlN ring are entirely separate from one another and both are supported via the Ni anchor, as shown in the far right cross-section of Fig. 8(j). Here, XeF_2 etches Mo fast and does not attack Al, Ni, or AlN. It is found that dehydration baking (120 °C for 20 min.) significantly improves the etch selectivity of Mo over oxide and nitride.

Fig. 8(j) also emphasizes a major advantage of this capacitive-piezo technology: Separation of electrodes and the

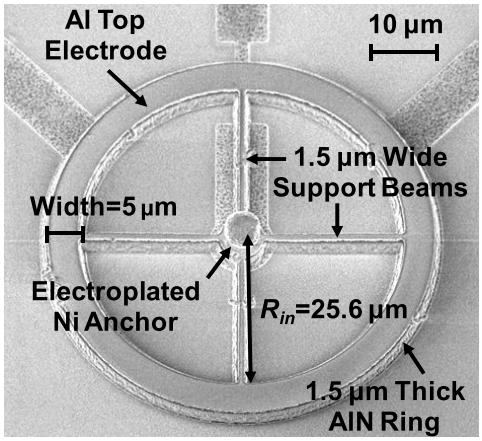

Fig. 11. Fabricated 1.2-GHz capacitive-piezo AlN ring resonator.

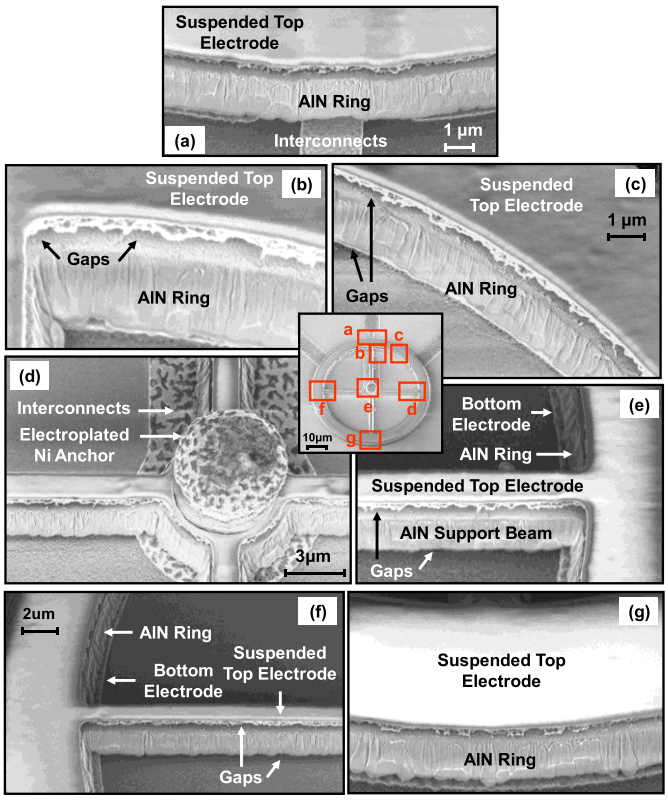

Fig. 12. SEM images at different parts of the same resonator confirming that the entire top electrode and the AlN ring resonator are suspended via the electroplated nickel anchor at the center. (a) Edge of the ring over interconnect to the center stem and top electrodes. (b) Gap between top electrode and ring at its inner edge near a support attachment point. (c) Gap between top electrode at ring at its inner edge. (d) Center stem anchor. (e) Top electrode on right side. (f) Top electrode on left side. (g) Ring edge showing top and bottom electrode-to-ring gaps.

AlN structure eliminate the Al-AlN-Al trimorph that otherwise ensues in conventional piezoelectric resonators, thereby avoiding issues commonly associated with bimorph and trimorph films, such as warping, stress relaxation, and film delamination.

Fig. 11 presents the wide-view SEM of a completed 1.2-GHz contour-mode e_{31}-capacitive-piezo-transduced ring resonator similar to the one depicted in Fig. 1. Fig. 12 presents SEM images of different parts of the same ring resonator delineating the gaps between the top/bottom electrode and the resonator. For these devices, to reduce electrode resistance, 400 nm thick Al is used as the top electrode—something that otherwise would not be permissible in a conventional AlN resonator, since its attached electrode would significantly mass load the resonant structure.

Although Al offers high conductance as an electrode material, which is good, its use does come with several disadvantages that might outweigh its conductivity advantages. In particular, (1) the RIE that defines AlN nitride structures also undercuts the Al top electrode—a problem that becomes more serious as the Al electrodes get thicker (to further reduce series resistance), since this provides a wider lateral diffusion path for etchants to undercut Al; (2) Al is highly reactive with other materials, causing problems at the interface of Al-Mo and Al-PECVD oxide even at low process temperature; and (3) Al sets the upper limit on process temperature if an anneal is desired to release stress, e.g., in the electroplated nickel anchor. Fortunately, alternative material sets are available that allow a process technology like that described, but without the use of Al. For example, one option might employ Mo as the electrode material, oxide as the sacrificial material, with the final release done via HF vapor.

VII. Experimental Results

To gauge the efficacy of the capacitive-piezo transducer at both high and low frequencies, layout for the described process flow included a 1.2-GHz contour-mode spoke-supported ring resonator, like that of [37], but this time in AlN; as well as a 50-MHz two-resonator array-composite [7], [14], [25] of wine-glass disks. Measured results for each of these are now presented.

A. 1.2-GHz Contour-Mode Ring Resonator

As shown in the SEM of Fig. 11, the width needed to achieve a resonance frequency of ∼1.2-GHz via a 1.5μm-thick AlN ring is 5μm. The 25.6μm inner radius of the ring is chosen to allow for quarter-wavelength supports that null energy losses to the anchor. Due to a need to enlarge the small center disk by 1.5μm in radius in order to allow proper lithography for stem electroplating, the supports for this device actually ended up being shorter than desired, and as will be seen, this impacts the attainable Q of this device.

Fig. 13 presents the measured frequency response characteristics for the AlN ring resonator of Fig. 11, showing a series resonance frequency $f_s = 1.23$GHz, $Q = 3,073$, and $R_x = 889\Omega$ at 3mTorr. Both the input and output are DC (not AC) grounded via bias-tee's to avoid electrostatic forces that might pull the top and bottom electrodes together and into the AlN resonator. Although the measured Q is still less than predicted by material loss theory, it is still higher than that of the majority of measured attached-electrode contour-mode AlN resonators at similar frequencies [45]–[47], although not all [16].

The measured series and parallel resonance frequencies yield a k^2_{eff} of 0.9%. Interestingly, this is considerably larger than the predicted value of 0.3% using the theory of Section V,

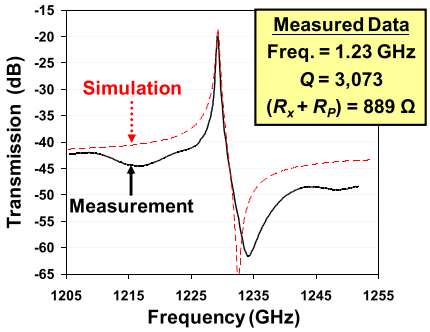

Simulated Parameters with Q=3,073

R_x	880	Ω
L_x	0.35	mH
C_x	0.048	fF
C_o	15.8	fF
(C_x/C_o)	0.3	%

Fig. 13. Measured frequency characteristic for a 1.2-GHz AlN ring resonator with dimensions as shown in Fig. 11 together with a simulation (dotted line) using the circuit of Fig. 6(c) with the predicted element values in the table to the right equivalent circuit of Fig. 6(c).

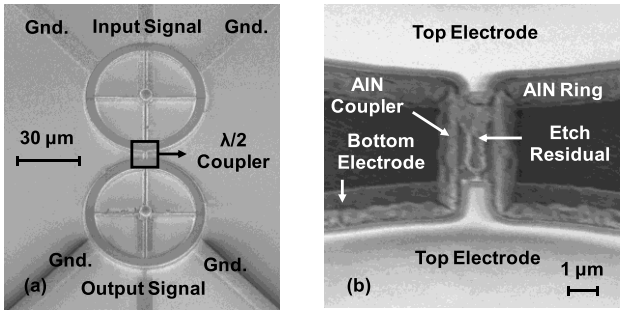

Fig. 14. (a) SEM of a capacitive-piezo ring resonator array with $\lambda/2$ coupler; and (b) top-view zoom-in SEM showing how the electrode is removed over the coupler to electrically isolate the output from the input.

which with some reduction in device width to match the series resonance frequency, yields the equivalent circuit elements and simulated plot also presented in Fig. 13. Smaller-than-expected electrode-to-resonator gap spacings can easily be responsible for the discrepancy. To lend some insight, if one assumes the $k^2_{eff,d=0}$ of AlN with no electrode gaps is 1.8%, then simple application of (30) with (4) yields an actual total gap spacing of 167nm, meaning the top and bottom gaps could be 84nm each. This very small value is possible, but somewhat surprising given the process flow of Section VI. It might be that the $k^2_{eff,d=0}$ of the AlN is higher than 1.8%, which as mentioned previously is plausible when metal is no longer attached to AlN, so no longer constrains its motion, allowing for a higher starting (gapless) $k^2_{eff,d=0}$ than so far exhibited by devices with actual attached electrodes. Whether due to smaller gaps or higher starting $k^2_{eff,d=0}$, the measured (C_x/C_o) is only slightly lower than that of conventional AlN resonators with contacting electrodes, and is actually higher than some. Whatever the case, it is sufficient for GHz narrow-band filters.

B. Two-Ring Array-Composite

To evaluate the efficacy of building mechanical circuits using capacitive-piezo transducers, two-ring mechanically half-wavelength coupled array-composites [7], one of which is shown in Fig. 14, were also fabricated and tested. Here, the top electrode over the coupling beam is removed to electrically isolate the output from the input. The measured frequency response from input ring to output ring,

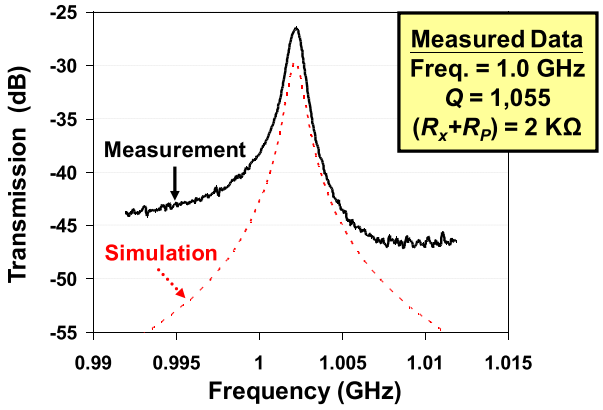

Fig. 15. Measured frequency characteristic for the resonator in Fig. 14 confirming suppression of the parallel resonance peak.

shown in Fig. 15, exhibits less feedthrough than seen in single-electrode devices, with parallel resonance suppressed as expected for a two-port device. However, the Q is lower for this mechanical circuit than for a single resonator, which might be caused by etch residuals atop the coupling beam formed after dry etching the top electrode, as shown in Fig. 14(b).

Unfortunately, these 1.2-GHz capacitive-piezo contour-mode ring resonator probably still do not reveal the intrinsic material Q of AlN. In particular, although the measured Q of 3,073 is already higher than many previously reported AlN-only piezoelectric rings, it is likely that anchor losses, not material losses, have the strongest role in dictating the Q. As mentioned, the original layout for the spoke-supported ring was overly aggressive in that it did not have sufficient overlap of the center disk around the center stem hole, which made lithography around the stem hole (for steps involved with stem-filling) very difficult. As a consequence, the mask for this portion had to be changed mid-process to increase the radius of the center disk. Although this facilitated stem hole lithography to the point of making the process possible, it also shifted the lengths of the spoke support beams so that they no longer were quarter-wavelength. As detailed in [6], without quarter-wavelength supports, spoke-supported ring resonator Q's suffer greatly.

It should be noted that designs featuring notched beam-to-ring attachments were also included on the ring layouts. These designs, first used in [37], attempt to attach the support beams at the ring nodal circle, which ideally does not move radially, so ideally would send no energy to the anchors whether or not the spoke support beams were quarter-wavelength. Unfortunately, multiple reflective metal layers of (*i.e.*, aluminum electrodes, nickel anchors, and molybdenum sacrificial) and heavy undercutting of the top metal layer in the fabrication process significantly complicated lithography, making it difficult to produce the ring notches needed for supports to attach at the nodal circle.

C. 50 MHz Two-Wine-Glass Disk Array-Composite

Fortunately, other structures capable of obviating the need for quarter-wavelength supports were also included in the

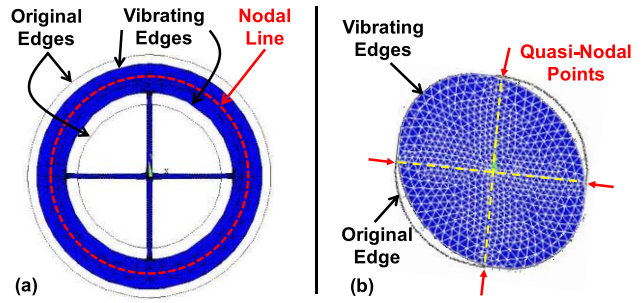

Fig. 16. (a) Mode shape of the contour-mode ring resonator shown in Fig. 11 and measured in Fig. 13. (b) Wine-glass mode shape with convenient access to the quasi-nodal points on the edge of the disk resonator, facilitating reduction of anchor loss to reveal the material Q of sputtered AlN.

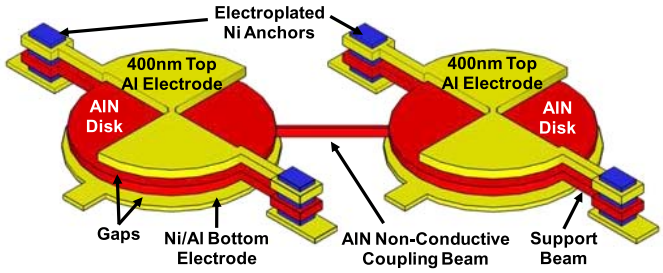

Fig. 17. An array-composite of two AlN disks employing capacitive-piezo transducers with non-contacting electrodes, drawn with exaggerated vertical gaps. The top electrodes are patterned for wine-glass mode resonance, for which quasi-nodal points can be accessed on the edges, as shown.

layout. In particular, structures designed to resonate in the wine-glass mode shape, in which the disk expands and contracts in opposite directions along orthogonal axes, have nodal lines shown in Fig. 16(b) that are accessible at points along the disk edge, obviating the need for the notches required by the previous contour-mode ring resonator and facilitating achievement of a Q-optimized design that can better expose the intrinsic material Q of AlN.

It should be mentioned that the wine-glass mode shape used here that facilitates Q-optimization also generates longitudinal and shear strains that are out-of-phase, thereby making it difficult to excite and sense the mode using the piezoelectric effect. Thus, although the devices of this work are good vehicles for tapping the Q of sputtered AlN, they are not so suitable for attaining low impedance. This also means that their output currents are small and not easily measured in the presence of feedthrough signals.

Like the ring device of Fig. 14, these devices employ half-wavelength coupled arrays [25] of disks, such as shown in Fig. 17. Here, uniform bottom and patterned top electrodes are spaced 260nm from the top and underside, respectively, of each AlN disk. The top electrodes make electrical contact to substrate interconnects through vias at the anchors. As detailed in [25], half-wavelength coupling effectively converts this device into a single composite device where constituent resonators vibrate together at one mode frequency, with little or no reduction in the overall Q of this mechanical circuit relative to that of a stand-alone device. The use of two devices in this mechanical circuit makes available two ports for interrogation: an input port to drive the device and an output port to sense its motion, both separated by a non-conductive

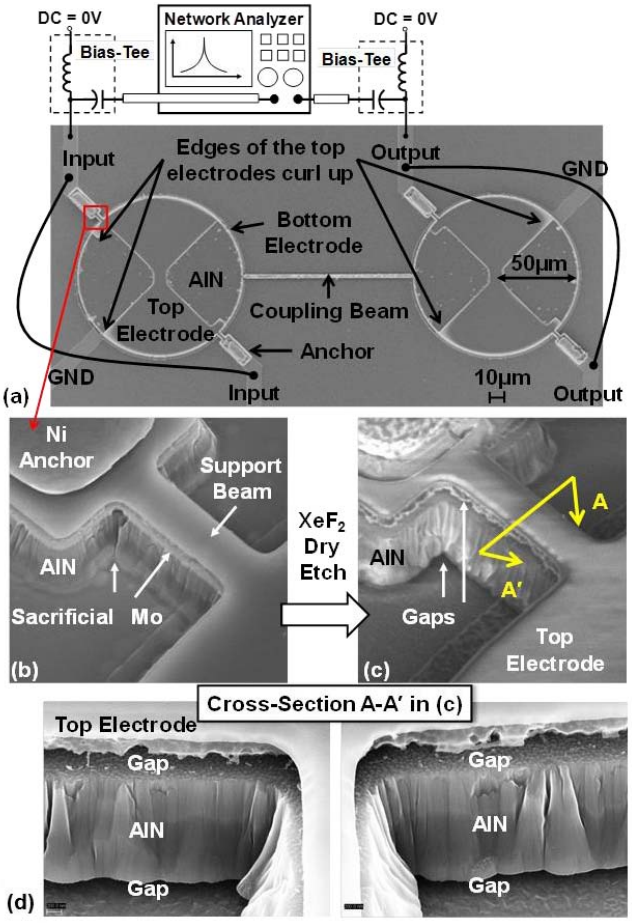

Fig. 18. (a) Fabricated AlN disk resonator array and the measurement setup that yields the measured frequency spectra in Fig. 20. (b), (c) Zoom-in views on the anchor before and after XeF_2 dry release, respectively. (d) Zoom-in on the suspended structure and electrodes, clearly showing the gaps.

AlN coupling beam that blocks feedthrough current, thereby greatly facilitating evaluation of piezoelectric wine-glass disks.

Fig. 18 presents the set-up used to measure the frequency characteristics for two-disk array-composites in (a), along with several SEMs showing the details of various parts of the device in the remaining figure parts. Here, the bottom electrodes of both resonators are grounded, while an AC input signal is applied to the top electrode of the left device and the output taken from that of the right. Again, although they sustain small AC signals, the input and output electrodes are DC grounded to prevent large electrostatic forces from pulling the top electrodes into contact with the AlN disks.

After XeF_2 release of devices, the following cleaning and annealing steps were taken, each of which noticeably and successively raised the Q's of the devices [20]:

1) Remove the photoresist that protects nitride/oxide isolation during release.
2) O_2 plasma, then dip in EKC-270 and perform critical point drying.
3) Anneal for 30 minutes in N_2/H_2 at 500 °C.

Fig. 20(a) presents frequency characteristics for two-disk array composite resonators employing various support beam widths (*cf.* Fig. 19) measured under 3 mTorr vacuum after the above steps. Here, resonators with support beam widths

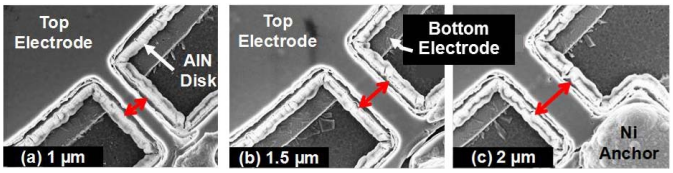

Fig. 19. Zoom-in SEMs of the support beams used in this work with various widths: (a) 1 μm; (b) 1.5 μm; (c) 2 μm.

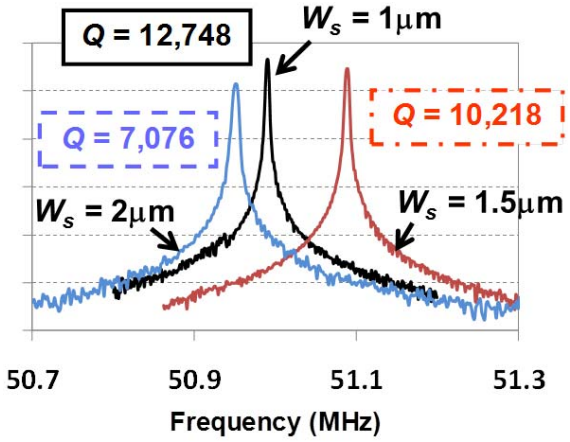

Fig. 20. Measured frequency characteristics for the resonators of Fig. 18 with various support beam widths after post-release clean and anneal procedures. That resonators with thinner support beams attain the highest Q indicates that anchor loss still dominates the Q, even for these wine-glass disks.

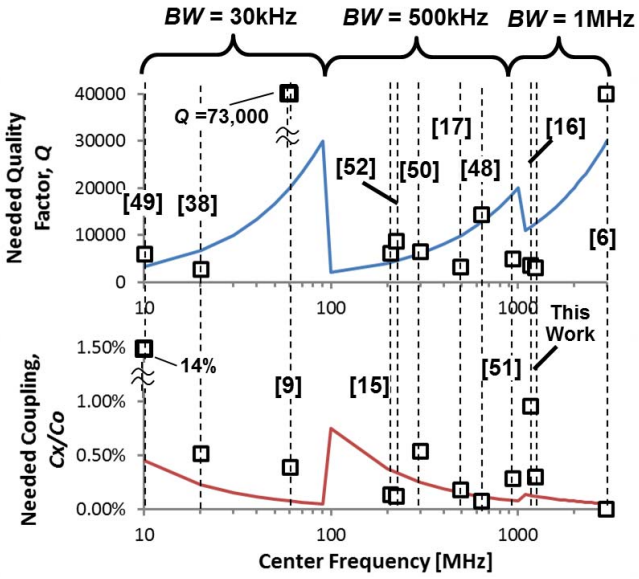

Fig. 21. Plot of needed Q and coupling (C_x/C_o) versus frequency for a sensible RF channel-select frequency allocation scheme with data points indicating marks achieved by various (cited) micromechanical resonator types.

of 2μm, 1.5μm, and 1μm, exhibit Q's of 7,076, 10,218, and 12,748, respectively, the last of which is the highest Q so far measured for sputtered thin-film AlN resonators. The rise in Q with shrinking support beam width suggests that anchor loss still plays an important role in determining Q for these wine-glass devices. Indeed, it is probable that the Q of 12,748 measured here is still shy of the intrinsic limit.

VIII. Conclusions

The described demonstration of a 1.2-GHz contour-mode AlN ring resonator with a motional resistance $R_x = 889\Omega$ and a $Q = 3,073$, together with that of a 50-MHz wine-glass disk with Q as high as 12,478, confirm the efficacy of capacitive-piezo transducers in raising the Q's of thin-film piezoelectric resonators. Indeed, the Q of 12,478 is so far the highest measured for any other d_{31}-transduced AlN-only thin-film piezoelectric resonator. Even so, there is evidence that it does not represent a Q ceiling, since anchor loss seems to still plague the measured devices. Improvements in fabrication, perhaps including the use of alternative materials for anchors and sacrificial layers to reduce the losses associated with anchors and etch residuals, may render even higher Q's.

Of course, Q is not the only important metric. As mentioned earlier, for the target RF channel-selecting front-end application [2], coupling (C_x/C_o) is equally important, as are aging stability, thermal stability, fabrication tolerances, on/off switchability, dynamic range, and numerous other difficult barriers. From a drift standpoint, the described capacitive-piezo devices should perform well, if BVA resonators are any indication. But keeping the focus on the most fundamental of the issues, Q and (C_x/C_o), one might ask how capacitive-piezo resonators measure up against other micromechanical resonator technologies in this application space. To answer this, Fig. 21 presents plots of needed Q and coupling (C_x/C_o) versus frequency for a sensible RF channel-select frequency allocation scheme. Here, legacy 30-kHz bandwidth channels span the 10-100 MHz range, 500-kHz channels span 100-1000 MHz, and 1-MHz channels span 1-3 GHz. The curves denoting the needed Q and (C_x/C_o) values are for two-resonator Chebyshev filters with 2 dB of insertion loss and less than 0.5 dB of passband distortion. As expected, needed Q's rise and needed (C_x/C_o)'s shrink as frequency increases within a given range. To support RF channel-selection, a given resonator must exceed both the needed Q and the (C_x/C_o) curves at its frequency.

From Fig. 21, the 1.2-GHz capacitive-piezo resonator of this work, perhaps encumbered by anchor loss, still does not satisfy the needs of RF channel-selection, as it lacks the needed Q. The 635-MHz quartz-MEMS device of [48] comes close, but does not quite satisfy the needed (C_x/C_o) value. In fact, of the twelve resonators plotted only three simultaneously satisfy the stated Q and (C_x/C_o) criteria: Two capacitive-gap transduced devices in the below 100 MHz regime [9], [49]; and one very recent capacitive-piezo disk device at 300 MHz [50]. This new capacitive-piezo device uses a different fabrication flow to achieve improved anchors, confirming that anchor losses constrain Q in the present devices. In addition, another recent lamb-wave capacitive-piezo device exhibits a $Q$of 5,019 at 941 MHz [51], showing best in class performance at UHF, although still not meeting the difficult Q requirement at this frequency. These recent devices further confirm the Q benefits and potential of capacitive-piezo resonator technology.

Acknowledgements

The authors would like to thank the Berkeley Microlab/Nanolab staff and members, especially Dr. X. Meng,

Dr. J. Black, Dr. P. Stephanou, and J. Donnelly, for their assistance and advice on fabrication.

REFERENCES

[1] A. Gasemi and E. S. Sousa, "Spectrum sensing in cognitive radio networks: Requirements, challenges and design trade-offs," *IEEE Commun. Mag.*, vol. 46, no. 4, pp. 32–39, Apr. 2008.

[2] C. T.-C. Nguyen, "Frequency-selective MEMS for miniaturized low-power communication devices," *IEEE Trans. Microw. Theory Techn.*, vol. 47, no. 8, pp. 1486–1503, Aug. 1999.

[3] C. T.-C. Nguyen, "Integrated micromechanical RF circuits for software-defined cognitive radio," in *Proc. 26th Symp. Sens., Micromach. Appl. Syst.*, Tokyo, Japan, Oct. 2009, pp. 1–5.

[4] K. Wang and C. T.-C. Nguyen, "High-order medium frequency micromechanical electronic filters," *J. Microelectromech. Syst.*, vol. 8, no. 4, pp. 534–557, Dec. 1999.

[5] R. A. Johnson, *Mechanical Filters in Electronics*. Hoboken, NJ, USA: Wiley, 1983.

[6] T. L. Naing *et al.*, "2.97-GHz CVD diamond ring resonator with Q>40,000," in *Proc. IEEE Int. Freq. Control Symp.*, Baltimore, MD, USA, May 2012, pp. 570–575.

[7] S.-S. Li, Y.-W. Lin, Z. Ren, and C. T.-C. Nguyen, "An MSI micromechanical differential disk-array filter," in *Proc. 14th Int. Conf. Solid-State Sens. Actuators (TRANSDUCERS)*, Lyon, France, Jun. 2007, pp. 307–311.

[8] T. J. Cheng and S. A. Bhave, "High-Q, low impedance polysilicon resonators with 10 nm air gaps," in *Proc. 23rd IEEE Int. Micro Electro Mech. Syst. (MEMS) Conf.*, Cancun, Mexico, Jan. 2010, pp. 695–698.

[9] M. Akgul, B. Kim, Z. Ren, and C. T.-C. Nguyen, "Capacitively transduced micromechanical resonators with simultaneous low motional resistance and Q>70,000," in *Solid-State Sens., Actuators, Microsyst. Workshop Tech. Dig.*, Hilton Head, CA, USA, Jun. 2010, pp. 467–470.

[10] K. Nai-Kuei *et al.*, "Micromachined sapphire GHz lateral overtone bulk acoustic resonators transduced by aluminum nitride," in *Proc. 25th IEEE Int. Micro Electro Mech. Syst. (MEMS) Conf.*, Paris, France, Jan./Feb. 2012, pp. 27–30.

[11] C.-M. Lin, Y.-Y. Chen, V. V. Felmetsger, D. G. Senesky, and A. P. Pisano, "AlN/3C–SiC composite plate enabling high-frequency and high-Q micromechanical resonators," *Adv. Mater.*, vol. 24, no. 20, pp. 2722–2727, May 2012.

[12] S. Gong, N.-K. Kuo, and G. Piazza, "GHz high-Q lateral overmoded bulk acoustic-wave resonators using epitaxial SiC thin film," *J. Microelectromech. Syst.*, vol. 21, no. 2, pp. 253–255, Apr. 2012.

[13] J. Masson *et al.*, "High overtone bulk acoustic resonators built using aluminum nitride thin films deposited onto AT-cut quartz plates," in *Proc. IEEE Int. Freq. Control Symp.*, Miami, FL, USA, Jun. 2006, pp. 835–838.

[14] Y.-W. Lin, L.-W. Hung, S.-S. Li, Z. Ren, and C. T.-C. Nguyen, "Quality factor boosting via mechanically-coupled arraying," in *Proc. Int. Solid-State Sens., Actuators, Microsyst. Conf. (TRANSDUCERS)*, Lyon, France, Jun. 2007, pp. 2453–2456.

[15] R. Abdolvand, H. M. Lavasani, G. K. Ho, and F. Ayazi, "Thin-film piezoelectric-on-silicon resonators for high-frequency reference oscillator applications," *IEEE Trans. Ultrason., Ferroelectr., Freq. Control*, vol. 55, no. 12, pp. 2596–2606, Dec. 2008.

[16] J. Segovia-Fernandez, N.-K. Kuo, and G. Piazza, "Impact of metal electrodes on the figure of merit ($kt^2 \cdot Q$) and spurious modes of contour mode AlN resonators," in *Proc. IEEE Ultrason. Symp.*, Dresden, Germany, Oct. 2012, pp. 299–302.

[17] C.-M. Lin, Y.-J. Lai, J.-C. Hsu, Y.-Y. Chen, D. G. Senesky, and A. P. Pisano, "High-Q aluminum nitride lamb wave resonators with biconvex edges," *Appl. Phys. Lett.*, vol. 99, no. 14, pp. 143501-1–143501-3, 2011.

[18] R. J. Besson, "A new 'electrodeless' resonator design," in *Proc. 31st IEEE Int. Freq. Control Symp.*, 1976, pp. 147–152.

[19] L.-W. Hung and C. T.-C. Nguyen, "Capacitive-piezo transducers for higher Q contour-mode AlN resonators at 1.2 GHz," in *Proc. Solid-State Sens., Actuators, Microsyst. Workshop*, Hilton Head, CA, USA, Jun. 2010, pp. 463–466.

[20] L.-W. Hung and C. T.-C. Nguyen, "Capacitive-Piezoelectric AlN resonators with Q>12,000," in *Proc. 24th IEEE Int. Conf. Micro Electro Mech. Syst. (MEMS)*, Cancun, Mexico, Jan. 2011, pp. 173–176.

[21] S. K. Kor, P. K. Mishra, and N. D. Tripathi, "Ultrasonic attenuation in pure and doped n-type silicon," *Phys. Rev. B*, vol. 10, no. 2, pp. 775–778, 1974.

[22] D. K. Pandey, D. Singh, and R. R. Yadav, "Ultrasonic wave propagation in IIIrd group nitrides," *Appl. Acoust.*, vol. 68, no. 7, pp. 766–777, 2007.

[23] R. Tabrizian, M. Rais-Zadeh, and F. Ayazi, "Effect of phonon interactions on limiting the f.Q product of micromechanical resonators," in *Solid-State Sens., Actuators, Microsyst. Conf. (TRANSDUCERS) Tech. Dig.*, Lyon, France, 2007, pp. 2131–2134.

[24] S. Gong, N.-K. Kuo, and G. Piazza, "GHz AlN lateral overmoded bulk acoustic wave resonators with a f·Q of 1.17 x 10^{13}," in *Proc. Joint IEEE Freq. Control Symp. Eur. Freq. Time Forum*, San Francisco, CA, USA, May 2011, pp. 1–5.

[25] Y.-W. Lin, S.-S. Li, Z. Ren, and C. T.-C. Nguyen, "Low phase noise array-composite micromechanical wine-glass disk oscillator," in *IEEE Int. Electron Devices Meet. (IEDM) Tech. Dig.*, Washington, DC, USA, Dec. 2005, pp. 287–290.

[26] F. Ayazi, S. Pourkamali, G. K. Ho, and R. Abdolvand, "High-aspect-ratio SOI vibrating micromechanical resonators and filters," in *Proc. IEEE MTT-S Int. Microw. Symp.*, San Francisco, CA, USA, Jun. 2006, pp. 676–679.

[27] S. V. Krishnaswamy, J. D. Adam, and M. Aumer, "P1J-4 high-Q FBARs using epitaxial AlN films," in *Proc. IEEE Int. Ultrason. Symp.*, Vancouver, BC, Canada, Oct. 2006, pp. 1467–1470.

[28] A. Frangi, M. Cremonesi, A. Jaakkola, and T. Pensala, "Analysis of anchor and interface losses in piezoelectric MEMS resonators," *Sens. Actuators A, Phys.*, vol. 190, pp. 127–135, Feb. 2013.

[29] C. G. Courcimault and M. G. Allen, "High-Q mechanical tuning of MEMS resonators using a metal deposition-annealing technique," in *13th Int. Conf. Solid-State Sens., Actuators, Microsyst. Conf. (TRANSDUCERS) Tech. Dig.*, Jun. 2005, pp. 875–878.

[30] T. Nishihara, T. Yokoyama, T. Miyashita, and Y. Satoh, "High performance and miniature thin film bulk acoustic wave filters for 5 GHz," in *Proc. Ultrason. Symp.*, Munich, Germany, Oct. 2002, pp. 969–972.

[31] C.-L. Huang, K.-W. Tray, and L. Wu, "Effect of AlN film thickness and top electrode materials on characteristics of thin-film bulk acoustic-wave resonator devices," *Jpn. J. Appl. Phys.*, vol. 44, no. 3R, pp. 1397–1402, 2005.

[32] M. Ueda *et al.*, "High-Q resonators using FBAR/SAW technology and their applications," in *Dig. IEEE Int. Microw. Symp.*, Long Beach, CA, USA, Jun. 2005, pp. 209–212.

[33] L. Mai, V.-S. Pham, and G. Yoon, "ZnO-based film bulk acoustic resonator devices on a specially designed Bragg reflector," *J. Appl. Phys. A*, vol. 95, no. 3, pp. 667–671, 2009.

[34] L. Lihua, P. Kumar, L. Calhoun, and D. L. DeVoe, "Piezoelectric $Al_{0.3}Ga_{0.7}As$ longitudinal mode bar resonators," *J. Microelectromech. Syst.*, vol. 15, no. 3, pp. 465–470, Jun. 2006.

[35] J. R. Norton and R. J. Besson, "Tactical BVA quartz resonator performance," in *Proc. 47th IEEE Int. Freq. Control Symp.*, Salt Lake City, UT, USA, Jun. 1993, pp. 609–613.

[36] T. Ikeda, *Fundamentals of Piezoelectricity*. New York, NY, USA: Oxford Univ. Press, 1990.

[37] S.-S. Li, Y.-W. Lin, Y. Xie, Z. Ren, and C. T.-C. Nguyen, "Micromechanical 'hollow-disk' ring resonators," in *Proc. 17th IEEE Int. Micro Electro Mech. Syst. Conf.*, Maastricht, The Netherlands, Jan. 2004, pp. 821–824.

[38] G. Piazza, P. J. Stephanou, and A. P. Pisano, "Piezoelectric aluminum nitride vibrating contour-mode MEMS resonators," *J. Microelectromech. Syst.*, vol. 15, no. 6, pp. 1406–1418, Dec. 2006.

[39] W. Pang, H. Zhang, H. Yu, C.-Y. Lee, and E. S. Kim, "Electrical frequency tuning of film bulk acoustic resonator," *J. Microelectromech. Syst.*, vol. 16, no. 6, p. 1303–1313, Dec. 2007.

[40] C. T.-C. Nguyen, "RF MEMS for channelizing low-power radios," in *Proc. 17th Int. Conf. Solid-State Sens., Actuators, Microsyst. (TRANSDUCERS)*, Barcelona, Spain, Jun. 2013, pp. 2455–2460.

[41] (2010, Jul. 1). *Micro Chem: LOR and PMGI Resists* [Online]. Available: http://184.168.52.107/pdf/PMGI-Resists-data-sheetV-rhcedit-102206.pdf

[42] J. Wang, J. E. Butler, T. Feygelson, and C. T.-C. Nguyen, "1.51-GHz nanocrystalline diamond micromechanical disk resonator with material-mismatched isolating support," in *Proc. 17th IEEE Int. Micro Electro Mech. Syst. Conf.*, Maastricht, The Netherlands, Jan. 2004, pp. 641–644.

[43] K. Wang, Y. Yu, A.-C. Wong, and C. T.-C. Nguyen, "VHF free-free beam high-Q micromechanical resonators," in *Proc. 12th Int. IEEE Micro Electro Mech. Syst. Conf.*, Orlando, FL, USA, Jan. 1999, pp. 453–458.

[44] J. R. Clark, W.-T. Hsu, M. A. Abdelmoneum, and C. T.-C. Nguyen, "High-Q UHF micromechanical radial-contour mode disk resonators," *J. Microelectromech. Syst.*, vol. 14, no. 6, pp. 1298–1310, Dec. 2005.

[45] C. Zuo, J. Van der Spiegel, and G. Piazza, "1.05 GHz MEMS oscillator based on lateral-field-excited piezoelectric AlN resonators," in *Proc. IEEE Int. Freq. Control Symp.*, Besancon, France, Apr. 2009, pp. 381–384.

[46] P. J. Stephanou and A. P. Pisano, "GHz higher order contour mode ALN annular resonators," in *Proc. IEEE 20th Int. Conf. Micro Electro Mech. Syst. (MEMS)*, Kobe, Japan, Jan. 2007, pp. 787–790.
[47] G. Piazza, P. J. Stephanou, and A. P. Pisano, "One and two port piezoelectric higher order contour-mode MEMS resonators for mechanical signal processing," *Solid-State Electron.*, vol. 51, no. 11, pp. 1596–1608, 2007.
[48] F. P. Stratton *et al.*, "A MEMS-based quartz resonator technology for GHz applications," in *Proc. IEEE Int. Freq. Control Symp. Expo.*, Montreal, QC, Canada, Aug. 2004, pp. 27–34.
[49] F. D. Bannon III, J. R. Clark, and C. T.-C. Nguyen, "High frequency micromechanical filters," *IEEE J. Solid-State Circuits*, vol. 35, no. 4, pp. 512–526, Apr. 2000.
[50] R. A. Schneider and C. T.-C. Nguyen, "On/off switchable high-Q capacitive-piezoelectric AlN resonators," in *Proc. IEEE 27th Int. Conf. Micro Electro Mech. Syst. (MEMS)*, San Francisco, CA, USA, Jan. 2014, pp. 1265–1268.
[51] T.-T. Yen, A. P. Pisano, and C. T.-C. Nguyen, "High-Q capacitive-piezoelectric AlN lamb wave resonators," in *Proc. IEEE 26th Int. Conf. Micro Electro Mech. Syst. (MEMS)*, Jan. 2013, pp. 114–117.
[52] M. Akgul and C. T.-C. Nguyen, "A passband-corrected high rejection channel-select micromechanical disk filter," in *Proc. IEEE Int. Freq. Control Symp.*, Taipei, Taiwan, May 2014, pp. 601–606.

Li-Wen Hung (S'04–M'12) received the B.S. degree in electrical engineering from National Taiwan University, Taipei, Taiwan, in 2005; the M.S. degree in electrical engineering and computer science from the University of Michigan, Ann Arbor, MI, USA, in 2006; and the Ph.D. degree in electrical engineering and computer science from the University of California at Berkeley, Berkeley, CA, USA, in 2011. While at Berkeley, she received multiple poster and presentation awards from the Berkeley Sensor and Actuator Center, and the Gold Prize TSMC Outstanding Student Research Award in 2010. Shortly after receiving the Ph.D. degree in 2011, she joined Invensense, San Jose, CA, USA, as a Research Engineer, where she explored RF-based products. In 2012, she joined IBM T. J. Watson Research Center, Yorktown Heights, NY, USA, where she is currently involved in research on sensors and 3-D packaging.

Clark T.-C. Nguyen (S'90–M'95–SM'01–F'07) received the B.S., M.S., and Ph.D. degrees from the University of California at Berkeley, Berkeley, CA, USA, in 1989, 1991, and 1994, respectively, all in electrical engineering and computer sciences.

He joined the faculty of the University of Michigan at Ann Arbor, Ann Arbor, MI, USA, in 1995, where he was a Professor with the Department of Electrical Engineering and Computer Sciences until 2006. In 2006, he joined the Department of Electrical Engineering and Computer Sciences at the University of California at Berkeley, where he is currently a Professor and the Co-Director of the Berkeley Sensor and Actuator Center. His research interests focus upon microelectromechanical systems (MEMS) including integrated micromechanical signal processors and sensors, merged circuit/micromechanical technologies, optomechanical devices, RF communication architectures, and integrated circuit design and technology. In 2001, he founded Discera, Inc., San Jose, CA, a company aimed at commercializing communication products based upon MEMS technology, with an initial focus on the very vibrating micromechanical resonators pioneered by his research in past years. He served as the Vice President and Chief Technology Officer of Discera until 2002, at which point he joined the Defense Advanced Research Projects Agency (DARPA) on an IPA, where he served for almost four years as the Program Manager of the MEMS, Micro Power Generation, Chip-Scale Atomic Clock, MEMS Exchange, Harsh Environment Robust Micromechanical Technology, Micro Gas Analyzers, Radio Isotope Micropower Sources, RF MEMS Improvement, Navigation-Grade Integrated Micro Gyroscopes, and Micro Cryogenic Coolers programs, in the Microsystems Technology Office of DARPA.

Dr. Nguyen received the Cady Award in 2006, and together with his students, has garnered more than 10 Best Paper Awards from IEEE conferences and journals focused on frequency control and MEMS. From 2007 to 2009, he served as a Distinguished Lecturer of the IEEE Solid-State Circuits Society. He was the Technical Program Chair of the 2010 IEEE International Frequency Control Symposium, and the Co-General Chair of the 2011 Combined IEEE International Frequency Control Symposium, and the European Frequency and Time Forum. From 2008 to 2013, he served as the Vice President of Frequency Control in the IEEE Ultrasonics, Ferroelectrics, and Frequency Control Society, and is currently the President-Elect of the same society.